Simulation of Carrier Injection Efficiency in AlGaN-Based UV-Light-Emitting Diodes

Gregor Hofmann, Anton Muhin , Norman Susilo , Friedhard Römer , Tim Wernicke, Michael Kneissl , *Fellow, IEEE*, and Bernd Witzigmann , *Senior Member, IEEE*

Abstract—**Numerical simulations of carrier transport in aluminium gallium nitride based ultraviolet light emitting diodes (UV-LED) are performed in order to understand injection efficiency for light sources in the deep ultraviolet. With our simulator, calibrated with experimental data from a 265 nm UV-LED, quantum efficiencies have been analyzed. The maximum internal quantum efficiency (IQE) of 30% consists of the product from radiative recombination efficiency (RRE) of 60% and carrier injection efficiency (CIE) of 50%. It is found that poor hole injection into the active region and a surplus of electrons limit both efficiencies, and leads to significant electron leakage into the p-side. This leakage is bias dependent, and has a minimum at maximum IQE. Further simulations show that distributed polarization doping (DPD) could improve carrier injection efficiency.**

Index Terms—**Efficiency, gallium nitride, LED, light emitting diode, light source, modeling.**

I. INTRODUCTION

LIGHT emitting diodes (LEDs) provide an efficient way to convert electrical to optical power. Aluminium gallium nitride (AlGaN) LEDs produce ultraviolet (UV) radiation with wavelengths as short as 210 nm [1]. UV emitters will improve environmental, medical and industrial application with their compactness and efficiency. Those applications include curing, sterilization and water purification [2]. Despite the recent advancements in AlGaN research, the external quantum efficiency (EQE) of UV-C LEDs is not comparable to visible LEDs yet [3]. The EQE, calculated by the product of carrier injection efficiency (CIE), the radiative recombination efficiency (RRE) and the light extraction efficiency (LEE) can be improved by increasing any of these efficiency factors. With the recent experimental evaluation of the CIE and RRE [4], simulations can complement the improvement of the efficiency not only by theoretical understanding but by developing models towards a predictive character. The investigation of the CIE from low to high current densities and the relation between the CIE and the

carrier dynamics in AlGaN UV-LEDs has not been investigated in detail. With a calibrated simulation, we evaluate the carrier transport in the active region (AR) by analyzing the quantum efficiencies and explaining the loss mechanisms. In addition, the effect of distributed polarization doping of the p-region is discussed.

II. OUTLINE

We first calibrate our simulation model to experimental data from a UV-LED emitting at 265 nm [4]. These data include electroluminescence (EL) spectra and the optical power at different current densities. From those, the iIQE, the CIE and the RRE can be extracted. With the calibration, several parameters in the model can be determined, which are the carrier recombination times, the inhomogeneous broadening parameter [5], the carrier mobility and an effective polarization. Subsequently, the quantum efficiencies and losses will be discussed.

III. SIMULATION SETUP

The geometry of the UV-LED is modelled in the TCAD environment *Sentaurus Workbench* by *SYNOPSYS* [6]. The calculations are carried out using a carrier transport model developed in [7]. It solves the drift and diffusion equations and the recombination processes in the quantum wells (QWs), with a special treatment of carrier transport in the QWs. They act as scattering centers for the continuum carriers [8]. The system of equations can be solved in 1- to 3-dimensions. For the simulations presented here, a 1-dimensional setup is used. Radiative recombination and spectral luminescence is computed only in the QWs by solving the Schrödinger equation based on a 6-band $\mathbf{k} \cdot \mathbf{p}$ theory for wurtzite structured semiconductors [9], [10]. Luminescence is calculated by spectral integration of transitions, with homogeneous and inhomogeneous broadening models as described in [5].

In Fig. 1, the device structure is shown. The layer sequence follows the LED heterostructure grown by metalorganic vapour-phase epitaxy. Starting from the n-side contact, a 100 nm thick n-type $Al_{0.68}Ga_{0.32}$ layer doped to 4×10^{18} cm^{-3} is followed by the active region (AR) containing three 1.4 nm thick $Al_{0.53}Ga_{0.47}$ QWs with adjacent $Al_{0.65}Ga_{0.35}$ quantum barriers (QB) of 5 nm thickness. The QB are n-doped to 4×10^{18} cm^{-3} as well. The AR contains an intentionally undoped 10 nm thick electron blocking layer (EBL) with an Al fraction of 86% between the last QB and the $Al_{0.76}Ga_{0.24}$ hole injection layer

	p-contact		
	GaN,	200 nm,	$N_A = 6 \times 10^{19}$ cm^{-3}
HIL	Al$_{0.76}$Ga$_{0.24}$N, 25 nm,		$N_A = 1 \times 10^{19}$ cm^{-3}
EBL	Al$_{0.86}$Ga$_{0.14}$N, 10 nm		
QB 3	Al$_{0.65}$Ga$_{0.35}$N, 10 nm		
QW 3	Al$_{0.53}$Ga$_{0.47}$N, 1.4 nm		
QB 2	Al$_{0.65}$Ga$_{0.35}$N, 5 nm,		$N_D = 4 \times 10^{18}$ cm^{-3}
QW 2	Al$_{0.53}$Ga$_{0.47}$N, 1.4 nm		
QB 1	Al$_{0.65}$Ga$_{0.35}$N, 5 nm,		$N_D = 4 \times 10^{18}$ cm^{-3}
QW 1	Al$_{0.53}$Ga$_{0.47}$N, 1.4 nm		
QB 0	Al$_{0.65}$Ga$_{0.35}$N, 40 nm,		$N_D = 4 \times 10^{18}$ cm^{-3}
	Al$_{0.68}$Ga$_{0.32}$N, 100 nm,		$N_D = 4 \times 10^{18}$ cm^{-3}
	n-contact		

(Active region: QB 3 through the Al$_{0.68}$Ga$_{0.32}$N, 100 nm layer)

Fig. 1. Simulation model of the device. The alloy composition, thickness and the doping concentration of each layer is shown. The active region is modelled with a background doping concentration of $N_A = 1 \times 10^{16}$ cm^{-3} and $N_D = 4 \times 10^{16}$ cm^{-3} − if not stated otherwise in the diagram.

(HIL). The device structure is completed by a p-GaN layer doped to 6×10^{19} cm^{-3}. The first, bottom n-layer of the device model is thinner compared to the UV-LED in the experiment. This doesn't change the outcome of the calculations. The layers are considered to be strained and lattice matched to AlN. The aluminium contents, the thicknesses and the doping concentration can also be taken from the block diagram in Fig. 1. In order to simulate light emission at 265 nm, the aluminium content in the QWs is fine-tuned to match the experimental data.

The doping profile in Fig. 1 follows data from secondary ion mass spectrometry (SIMS) of the device. The doping concentrations N_D and N_A describe the donor and acceptor density, respectively. Si acts as the main donor and Mg as the main acceptor species. The dopants are incorporated with an alloy dependent ionization rate, using an activation model [11]. Activation depends on the local carrier density following a Shockley model, and the activation rate includes enhancement due to proximity and field effects [12]. The energy level of Si is 30 meV in GaN and 65.1 meV in Al$_{0.68}$Ga$_{0.32}$N. The energy level of Mg is 245 meV in GaN and 630 meV in AlN [1], [13], [14], [15]. For the ternary alloys, the energy levels are interpolated linearly. Also, for the Mg doping we take into account that residue hydrogen atoms deactivate the capability of Mg to provide holes [16].

Basic material parameters are taken from literature [17], unless noted otherwise. At room temperature, the bandgap energy for GaN is 3.437 eV and the bandgap energy for AlN is 6.1 eV. We choose a global bandgap bowing parameter of $b = 1.1$ eV [18], [19]. The electron mobility μ_e is modelled by the Arora model [20]. The hole mobility μ_h is assumed to be constant across the device heterostructure. The simulation temperature is 300 K. Recent pyroelectric material parameters for wurtzite materials are used [21]. The spontaneous and piezoelectric polarization value is scaled with an effective polarization parameter p_{eff} to account for alloy fluctuations and surface states [22].

The threading dislocation density (TDD) is set to $N_{TDD} = 1 \times 10^9$ cm^{-2} in the device [4] and acts as non-radiative recombination term [23]. Another non-radiative recombination terms is the Shockley-Read-Hall (SRH) recombination at point defects. Hereby, we use recombination times τ_e^{SRH} for electrons and τ_h^{SRH} for holes, which are independent of the aluminium content. Additionally, we assume non-radiative Auger-Meitner recombination [24], [25], [26] using calibrated data from a previous work [7]. The scattering parameters for the carrier capture model into the QWs [7] have been set to $\tau_{e/h} = 5/1$ ps for electrons and holes, respectively.

IV. COMPARISON TO EXPERIMENT

For the calibration of the parameters, the carrier recombination times τ_e^{SRH} and τ_h^{SRH}, the inhomogeneous broadening parameter σ_{IHB}, and the hole mobility μ_h are adjusted to match the experimental data. Experimental data for the electroluminescence (EL) spectra and optical power versus current density are available, from the devices published in [4]. The measurements have been taken in pulsed mode, and the efficiencies taken from mounted LEDs. The parameters have been chosen as follows in order to calculate the results in this paper: the defect related SRH carrier recombination times are set to $\tau_e^{SRH} = 3$ ns and $\tau_h^{SRH} = 5$ ns, which is the inverse of the A-parameter in a rate equation model. These values are close to PL characterization of similar structures, where a non-radiative lifetime of $\tau^{nr} = 3$ ns has been extracted at room temperature [27]. The inhomogeneous broadening parameter is chosen as $\sigma_{\text{IHB}} = 100$ meV, and the hole mobility set to $\mu_h = 2$ cm^2/V/s. The effective polarization at the hetero interfaces has been set to $p_{eff} = 50\%$, which accounts for alloy fluctuations and charged impurities within this model.

A. EL Spectrum

The EL spectra in Fig. 2 shows the simulated (lines) compared to the measured data (dots) for a variation of current densities. The main parameter is the inhomogeneous broadening which is set to $\sigma_{\text{IHB}} = 100$ meV, close to the values obtained in [5]. Compared to the device sample sheet, the aluminium content in the active region is increased by 3% in order to match the peak wavelength. The low energy side of the spectrum shows some deviation, and requires future refinement of the model. The simulated spectra are normalized to the peak of the experimental spectrum, measured at $J = 100$ Acm^{-2}. In the simulation, only the TE polarization of the emission is plotted, which represents the measured data. The simulated degree of polarization (DoP), which consists of the ratio $(I_{TE} - I_{TM})/(I_{TE} + I_{TM})$ has been calculated to 82%, which is in good agreement to experiment [28]. The simulations replicate the negligible peak shift with increasing current density showing that neither band filling nor screening of polarization fields affect the emission wavelength in the investigated current density range. Due to the n-doping in the barriers the electron concentration in the quantum wells is almost constant and ten times larger than the hole density for the investigated current densities. As the electrons govern band filling and screening the emission wavelength
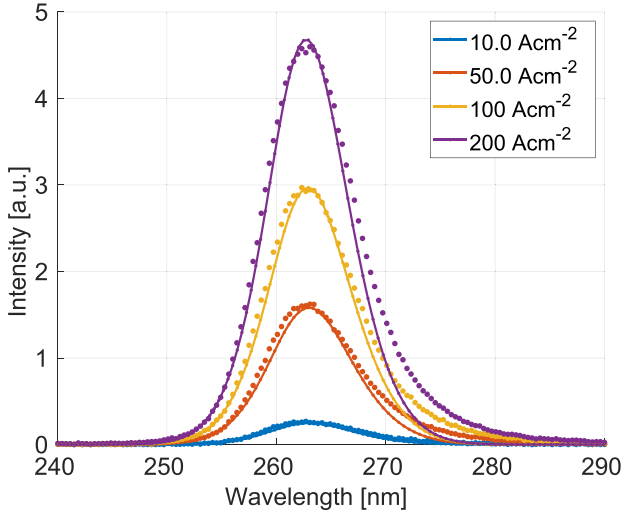
Fig. 2.   Simulated spectra (line) compared to a EL measurements (dots, [4]) for the current densities shown in the legend. The simulated intensity is normalized to the peak of the $J = 100$ Acm^{-2} spectrum, and the simulated DoP is 82%.
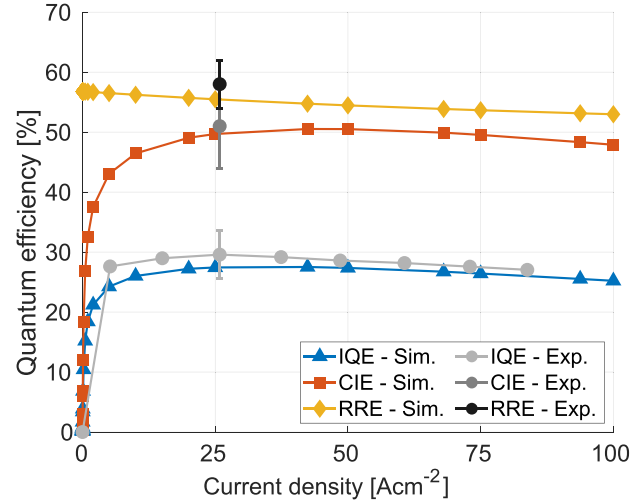

Fig. 3.   Efficiency diagram of a simulated 265 nm LED for varying current densities. The yellow curve is the average RRE from the QWs. Red is the CIE. Blue is the IQE. Black and grey circles indicate experimental values [4].

stays constant. The hole densities govern the recombination rates causing the increasing emission intensities.

B. Electro-Optical Efficiency

The device EQE η^{EQE} associates the optical power density P to the current density J. The EQE can be expressed as follows:

$$\eta^{EQE} = \frac{qP}{E_{ph}J} = \eta^{LEE}\eta^{IQE} = \eta^{LEE}\eta^{CIE}\eta^{RRE}. \quad (1)$$

Here q is the electron charge, E_{ph} is the photon energy averaged over the LED emission spectrum, and η^{LEE} is the light extraction efficiency (LEE). The LEE η^{LEE} was calculated by calibrated ray tracing simulations as described in [29] and [4], and is used in our simulation as well. Additionally η_{exp}^{RRE} was determined by a modified ABC-model fit in [4] allowing to calculate the peak RRE and subsequently the peak CIE. Therefore we can compare the calculated efficiencies to the experimentally derived efficiencies

$$\eta_{exp}^{IQE} = \frac{\eta_{exp}^{EQE}}{\eta_{exp}^{LEE}} = \eta_{exp}^{CIE}\eta_{exp}^{RRE}. \quad (2)$$

Our simulator calculates the quantum efficiencies η^{CIE} and η^{RRE} directly from the microscopic model. The CIE is defined by the fraction of carriers that recombine inside the QW, and is obtained from

$$\eta_{sim}^{CIE} = J_{QW}/J, \quad (3)$$

where J_{QW} the current density injected into the QWs of the LED. The RRE is evaluated by

$$\eta_{sim}^{RRE} = J_{rad}/J_{QW}. \quad (4)$$

Here, J_{rad} is the current density from radiative recombination in the QW. The IQE is calculated by

$$\eta_{sim}^{IQE} = J_{rad}/J. \quad (5)$$

The IQE is then

$$\eta_{sim}^{IQE} = \eta_{sim}^{CIE}\eta_{sim}^{RRE}. \quad (6)$$

Equation (6) can be compared to the experimental efficiency data in (2).

In Fig. 3, the simulated measured efficiencies are shown for current densities up to 100 mA/cm^2. At $J = 25$ Acm^{-2}, the IQE maximum reaches 30%, and drops for higher values.

This efficiency drop at higher optical power is still being investigated [4], [7], [30], [31]. For analysis purpose, the EQE η^{EQE} can also be plotted versus the normalized optical power p, where

$$p = \frac{P}{P_{max,IQE}} \quad (7)$$

is calculated by the optical power P divided by the optical power at peak IQE $P_{max,IQE}$. This transfer characteristic is shown in Fig. 4. The peak IQE is reached at $p = 1$, corresponding to $J = 25$ Acm^{-2} for both the experiment and the simulation, as seen in Fig. 3. We assume η^{LEE} to be independent from the optical power density p and we use (1) to calculate the EQE.

In summary, good agreement between experiment and simulation has been obtained by with our model.

V. CARRIER TRANSPORT IN SIMULATION

Based on the calibration of the simulation model to experimental quantities in Figs. 2, 3 and 4, internal device physics such as the carrier distributions can now be analyzed.

A. Carrier Distribution

Fig. 5 shows calculated electron and hole density distribution for the current densities at $J = 1, 25, 100$ Acm^{-2}, with $J = 25$ Acm^{-2} being the IQE maximum. In the figure, the device layers are indicated by the shading of the background.
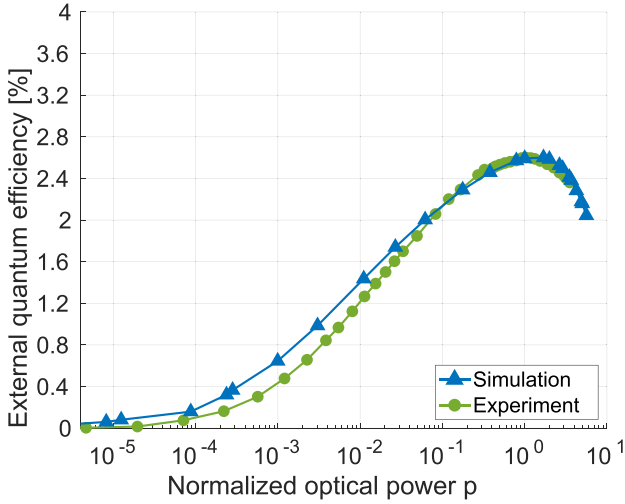
Fig. 4. Dependency of the EQE on the normalized optical power parameter p. Comparing the simulation data (blue) to experimental data (green) [4].
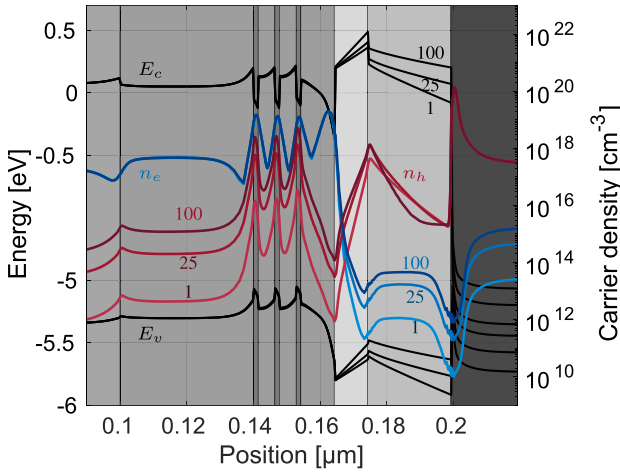

Fig. 6. Simulation of ionized donor and acceptor density at a current density $J = 25$ Acm^{-2}. The blue line indicates the ionized donor N_D^* and red the ionized acceptor density N_A^*. The percentages show relative magnitude of ionized dopants in the respective layers.

Fig. 5. Simulation of band structure and carrier densities at different current densities $J = 1, 25, 100$ Acm^{-2}. The background color represents the layers, (see Fig. 1). The thick black lines are the conduction/valence band energies, and the blue/red lines the electron/hole densities.

In the QWs, a strong imbalance of the carrier species is present. At the IQE maximum, the electron density reaches $n_e = 1.8 \pm 0.2 \times 10^{19}$ cm^{-3}, while the maximum hole density only reaches $n_h = 8.2 \pm 0.9 \times 10^{17}$ cm^{-3}. Also, with rising current, the QW electron density stays nearly constant, and only the hole density rises: from $J = 1$ Acm^{-2} to $J = 100$ Acm^{-2} the hole density rises from $n_h = 1.7 \pm 0.8 \times 10^{16}$ cm^{-3} to $n_h = 2.7 \pm 1.0 \times 10^{18}$ cm^{-3}. Clearly, a lack of holes in the active region prevents efficient UV-LED operation.

A major factor for the lack of holes in the QWs is the high ionization energy of Mg acceptors in AlGaN. Fig. 6 shows the ionized dopant density in the device for donor N_D^* and acceptor N_A^* densities.

At the n-side, the donors are ionized to at 45% of the impurity density. The n-layers therefore possess a low resistance and good electron injection in the active region. At the p-side, despite
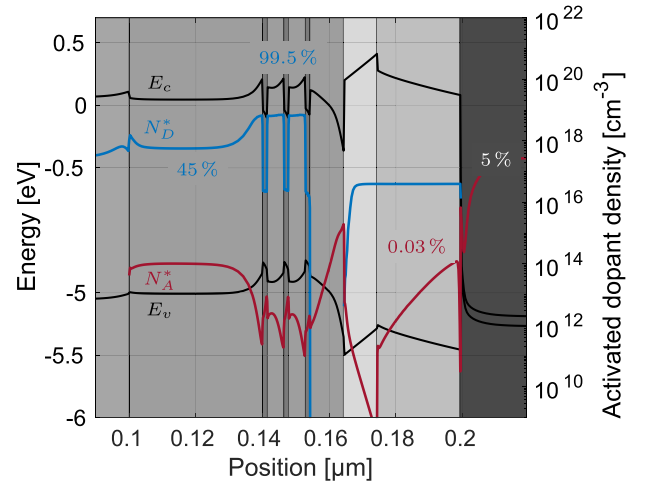
a high doping concentration of acceptors, only a tiny fraction $< 5\%$ of the acceptors provide free holes and contribute to the overall carrier transport. The HIL with an Al content of 76% and Mg concentration of 1×10^{19} cm^{-3} is ionized by 0.03%, which leads to the low density shown in Fig. 5. Achieving a high density of mobile holes in AlGaN devices is ongoing research and still a technological challenge [32], [33]. Another issue is the hetero interface between the last thick barrier layer and the EBL with a high Al content of 86%. The positive polarization charge attracts electrons (similar to the channel in a HEMT structure), pulling down the energy bands. This leads to a high barrier for the injection of holes, and to strong recombination close to this interface due to the high electron density.

Within the three QWs, the carrier distribution is relatively homogeneous. At each QW interface, polarization charges create an electric field in the barriers and wells, which tilts the bands. In the barriers, this field introduces an additional electrostatic potential spike of approx. 60 meV between the wells. In the current design, the barriers are doped with Si (n-type), and at LED operation, the ionized immobile donors have a positive charge. As a consequence, the bands in the barriers are curved, which facilitates electron transport through the MQW structure.

B. Quantum Efficiencies

The maximum IQE at 30% consists of the product of the RRE $\eta_{RRE} \approx 60\%$ and the CIE $\eta_{CIE} \approx 50\%$, with the latter being strongly current dependent (see Fig. 3). Both contributions are now described in more detail.

1) Radiative Recombination Efficiency: The RRE describes the ratio of radiative recombination to total recombination for the carriers in the QWs. In Fig. 3 the RRE versus current starts at 58% and drops to 50% at current densities of 200 A/cm^2 (not shown). In the low current regime, the SRH rate $R_{e,h}^{SRH}$ is the main contributor of non-radiative recombination. The large
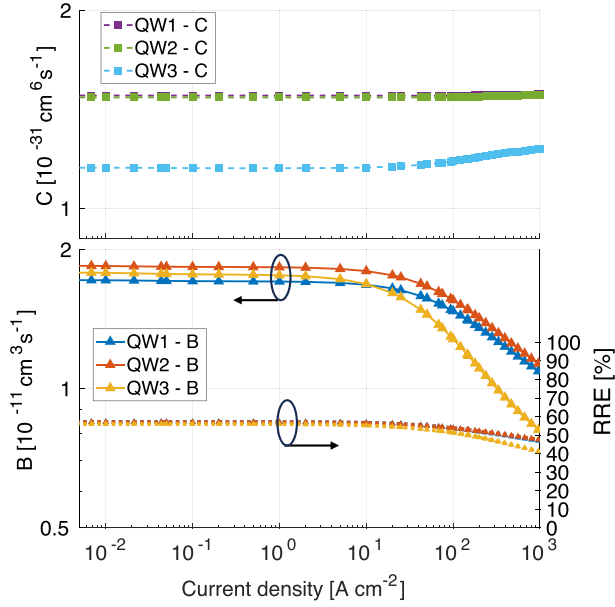
Fig. 7. Effective B- and C-coefficient as calculated from the microscopic simulation (left axes), and RRE for the 3 QWs (QW1-3 from n-side to p-side).
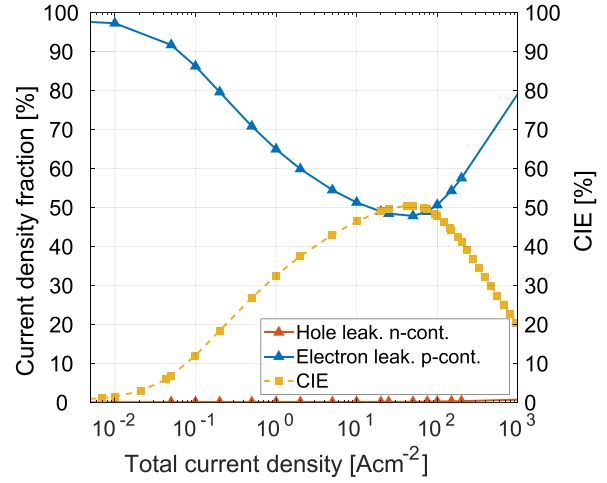

Fig. 8. Simulation of the electron current density J_e reaching the p-contact, the hole current density J_h reaching the n-contact and the overall CIE for a variation of the total current density $J = J_e + J_h$.

imbalance of electron to hole density leads to a high electron SRH rate, as many electrons can recombine non-radiatively. They lack a corresponding hole state for radiative bi-molecular recombination. The SRH rate at lowest current densities is also influenced by trap assisted tunneling, as shown in [34]. Additional calculations (not included here) show that the overall RRE has strongly depends on the hole SRH rate, as it limits the bimolecular radiative recombination. In Fig. 7 effective B- and C-coefficients are extracted from the simulations (with QW1 on the n-side and QW3 on the p-side). The extraction of the coefficients is done by taking the respective recombination rate, calculated from the microscopic simulation, and, in the case of the B-coefficient, dividing the rate by the product of electron and hole density. The same procedure is applied for the Auger-Meitner C-coefficient. In a rate equation model, the coefficients would be constant at all densities or currents. In our simulation, they are dependent on current density due to phase space filling effects [35] and change of wave function overlap between the QW states. In Fig. 7, the B-coefficient decreases and the C-coefficient increases at high current densities. The latter is due to the increased wave function overlap in the QWs. The decrease of B is from phase space filling, a combination of non-parabolic band dispersion and use of Fermi-Dirac carrier distributions. The decrease of the RRE with current follows the decrease of the B-coefficient. In general, the values of B- and C-coefficient are in good agreement with atomistic calculations in [25]. On the other hand, fitting the measured efficiencies to ABC-models result in larger coefficients for B and C (see e.g. [4]), which can be explained by the unipolar approximation and missing CIE in the ABC model.

2) Carrier Injection Efficiency (CIE): The CIE determines how many carriers injected into the semiconductor enter the QWs. For the calibrated UV-LED structure, the CIE can be

extracted by measuring the minority currents close to the AR, which represent the leakage currents from the QWs. Even in an ideal case, the leakage is not zero, as any pn-diode with finite thickness exhibits minority currents. Fig. 8 plots the CIE and the respective leakage currents in the LED for electrons and holes versus current density. At low currents, the electron leakage is almost 100%. This is due to high barriers at the p-side between the GaN, HIL and EBL, and the low conductivity of these layers, which prevent any significant hole injection into the device (see also Fig. 5). The UV-LED is almost unipolar, with electron current flowing from the n- to the p-contact. At these low currents, there is however a small hole current leading to electron and hole density in the QWs, and it is possible to generate RRE of close to 60%.

Increasing the potential difference between the contacts results in a larger hole current through the p-doped AlGaN layers, and the hole density in the QWs leads to higher radiative recombination. Hence, the CIE rises to a maximum of 51%. At higher currents, electron leakage sets in again, as the QWs are saturated with electrons, resulting in the IQE efficiency droop. Parameter variations in the simulations show that the CIE can be increased by increasing the hole mobility or the p-dopant levels in the HIL to values of $p_{dop} = 1 \times 10^{20}$ cm^{-3}. Both measures are difficult to realize technologically, in addition to being contradictory, as higher impurity density harms the mobility in general. These results underline the importance of improving hole injection into the active region.

VI. DISTRIBUTED POLARIZATION DOPING (DPD)

One way to improve the hole injection into the active region is to employ layers with graded aluminium fractions, which leads to immobile volume charges due to the polarization gradient in the polar crystal. Details can be found in [36], [37], [38]. Here, the HIL is replaced by a nominally undoped layer with aluminium grading from $x = 86\%$ to $x = 65\%$, creating an immobile polarization charge density of $n_{pol} = 2.5 \times 10^{18}$ cm^{-3} within the thickness of 25 nm, and a mobile hole density of the
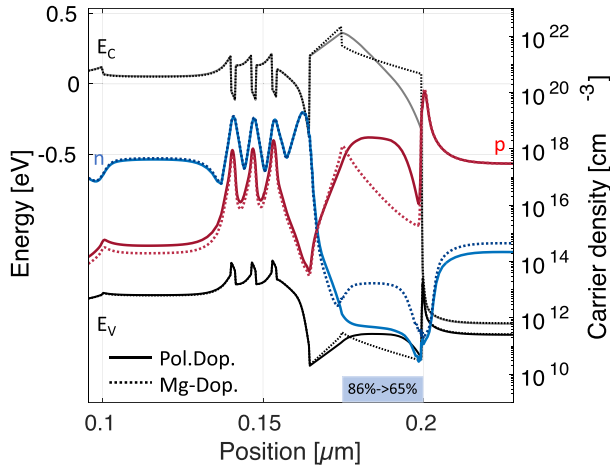
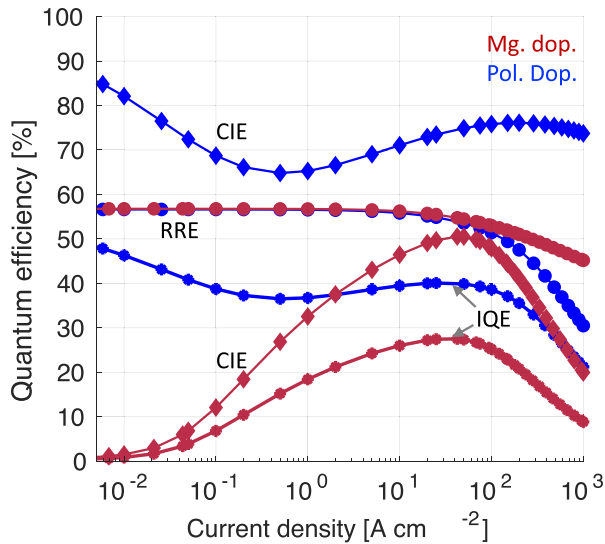Fig. 9.   Band energy plot and carrier densities for an LED with with DPD versus standard Mg doped design.

Fig. 10.   Simulation of CIE, RRE, and IQE for a UV LED with DPD layer (blue) versus magnesium doped p-layer (red).

and IQE are plotted, again comparing the calibrated structure (red curves) versus the DPD structure (blue curves). Due to the improved conductivity at the p-side, the CIE is almost constant between 90% at low current densities to 70% at current densities above $J = 10$ Acm^{-2}. This leads to a substantial improvement of the IQE, which is around 40% at typical operating current densities. RRE decreases more strongly at high currents due to phase space filling. At low currents, the hole injection bottleneck disappeared, as much less voltage is necessary to supply holes to the active region.

VII. CONCLUSION

Analysis of the carrier injection efficiency (CIE) in AlGaN-based UV-LEDs using a carrier transport simulation has been presented. The model has been calibrated with experimental data from a UV-LED emitting at 265 nm. It has been found that a low hole density in the p-doped layers by Mg doping with high activation energies is the main challenge. Lack of holes in the active region and n-doping of the barriers leads to a surplus of electrons, and their non-radiative recombination reduces the radiative recombination efficiency. In addition, high barriers in the valence band at the p-side prevent hole injection at low current densities, leading to high minority currents of electrons at the p-contact, resembling a unipolar device. This is the main reason for the strong current dependence of the IQE observed in experiments. As a solution, distributed polarization doping can increase the IQE maximum from 30% to above 40%, which should be considered in further designs.

Conflict of Interest: The authors declare no conflict of interest.

Data Availability Statement: The data that support the findings of this study are available from the corresponding author upon reasonable request.

same magnitude. In the simulation, this is calculated by taking the divergence of the local polarization as preprocessing step. For comparison, the reference structure possesses an HIL with Mg doping of $p_{dop} = 1 \times 10^{19}$ cm^{-3}, and Al content of 76%.

Fig. 9 shows the band structure and carrier densities at a current density of $J = 25$ Acm^{-2}, with solid lines being the DPD case and dashed lines the calibrated reference structure. For the DPD structure, the hole density in the HIL reaches the charge density induced by the polarization gradient, which leads to a layer with low resistance. As a consequence, the active QW hole density rises from $p = 1.5 \pm 4.0 \times 10^{17}$ cm^{-3} (Mg doped) to $p = 1.5 \pm 0.5 \times 10^{18}$ cm^{-3} (DPD). The DPD layer leads to a doubling of the hole density and a much reduced inhomogeneity of the carrier distribution in the MQW structure.

The improved hole injection modifies the efficiencies of the UV-LED structure. In Fig. 10 the current dependent CIE, RRE

REFERENCES

[1] Y. Taniyasu, M. Kasu, and T. Makimoto, "An aluminium nitride light-emitting diode with a wavelength of 210 nanometres," *Nature*, vol. 441, no. 7091, pp. 325–328, 2006.

[2] M. Kneissl, T.-Y. Seong, J. Han, and H. Amano, "The emergence and prospects of deep-ultraviolet light-emitting diode technologies," *Nature Photon.*, vol. 13, no. 4, pp. 233–244, 2019.

[3] H. Amano et al., "The 2020 UV emitter roadmap," *J. Phys. D: Appl. Phys.*, vol. 53, no. 50, Sep. 2020, Art. no. 503001, doi: 10.1088/1361-6463/aba64c.

[4] A. Muhin et al., "Radiative recombination and carrier injection efficiencies in 265 nm deep UV LEDs grown on ALN/sapphire templates with different defect densities," *Physica Status Solidi A*, vol. 220, no. 16, pp. 2200458–2200465, 2022.

[5] F. Römer, M. Guttmann, T. Wernicke, M. Kneissl, and B. Witzigmann, "Effect of inhomogeneous broadening in ultraviolet III-nitride light-emitting diodes," *Materials*, vol. 14, no. 24, 2021, Art. no. 7890.

[6] Synopsys, "Sentaurus workbench," 2023. [Online]. Available: https://www.synopsys.com/

[7] F. Römer and B. Witzigmann, "Effect of auger recombination and leakage on the droop in InGaN/GaN quantum well LEDs," *Opt. Exp.*, vol. 22, no. S6, 2014, Art. no. A1440.

[8] G. A. Baraff, "Semiclassical description of electron transport in semiconductor quantum-well devices," *Phys. Rev. B*, vol. 55, pp. 10745–10753, Apr. 1997, doi: 10.1103/PhysRevB.55.10745.

[9] S. L. Chuang and C. S. Chang, "kp method for strained wurtzite semiconductors," *Phys. Rev. B*, vol. 54, pp. 2491–2504, Jul. 1996, doi: 10.1103/PhysRevB.54.2491.

[10] S.-H. Park and S.-L. Chuang, "Crystal-orientation effects on the piezoelectric field and electronic properties of strained wurtzite semiconductors," *Phys. Rev. B*, vol. 59, pp. 4725–4737, Feb. 1999, doi: 10.1103/PhysRevB.59.4725.

[11] W. Götz, R. Kern, C. Chen, H. Liu, D. Steigerwald, and R. Fletcher, "Hall-effect characterization of III–V nitride semiconductors for high efficiency light emitting diodes," *Mater. Sci. Eng.: B*, vol. 59, no. 1, pp. 211–217, 1999. [Online]. Available: https://www.sciencedirect.com/science/article/pii/S0921510798003936

[12] F. Römer and B. Witzigmann, "Acceptor impurity activation in III-nitride light emitting diodes," *Appl. Phys. Lett.*, vol. 106, no. 2, Jan. 2015, Art. no. 021107, doi: 10.1063/1.4905870.

[13] X. T. Trinh, D. Nilsson, I. G. Ivanov, E. Janzén, A. Kakanakova-Georgieva, and N. T. Son, "Stable and metastable si negative-u centers in AlGaN and ALN," *Appl. Phys. Lett.*, vol. 105, no. 16, Oct. 2014, Art. no. 162106, doi: 10.1063/1.4900409.

[14] P. Paskov, B. Monemar, A. Toropov, P. Bergman, and A. Usui, "Two-electron transition spectroscopy of shallow donors in bulk GAN," *Physica Status Solidi (C)*, vol. 4, pp. 2601–2604, Jun. 2007.

[15] S. Brochen, J. Brault, S. Chenot, A. Dussaigne, M. Leroux, and B. Damilano, "Erratum: "Dependence of the MG-related acceptor ionization energy with the acceptor concentration in p-type GAN layers grown by molecular beam epitaxy"," *Appl. Phys. Lett.*, vol. 103, no. 26, Dec. 2013, Art. no. 269904, doi: 10.1063/1.4858978.

[16] J. L. Lyons, A. Janotti, and C. G. Van de Walle, "Shallow versus deep nature of MG acceptors in nitride semiconductors," *Phys. Rev. Lett.*, vol. 108, Apr. 2012, Art. no. 156403, doi: 10.1103/PhysRevLett.108.156403.

[17] E. Bellotti and F. Bertazzi, "Transport parameters for electrons and holes," in *Nitride Semiconductor Devices Principles and Simulation*. Hoboken, NJ, USA: Wiley, 2007, ch. 4, pp. 69–93, doi: 10.1002/9783527610723.ch4.

[18] V. Jmerik et al., "AlGaN quantum well structures for deep-uv LEDs grown by plasma-assisted MBE using sub-monolayer digital-alloying technique," *J. Cryst. Growth*, vol. 311, pp. 2080–2083, Mar. 2009.

[19] Z. Li et al., "Plasma assisted molecular beam epitaxy growth mechanism of AlGaN epilayers and strain relaxation on ALN templates," *Japanese J. Appl. Phys.*, vol. 60, Jun. 2021, Art. no. 075504.

[20] N. Arora, J. Hauser, and D. Roulston, "Electron and hole mobilities in silicon as a function of concentration and temperature," *IEEE Trans. Electron Devices*, vol. ED-29, no. 2, pp. 292–295, Feb. 1982.

[21] C. E. Dreyer, A. Janotti, C. G. Van de Walle, and D. Vanderbilt, "Correct implementation of polarization constants in wurtzite materials and impact on iii-nitrides," *Phys. Rev. X*, vol. 6, Jun. 2016, Art. no. 021038, doi: 10.1103/PhysRevX.6.021038.

[22] O. Ambacher et al., "Two dimensional electron gases induced by spontaneous and piezoelectric polarization in undoped and doped AlGaN/GAN heterostructures," *J. Appl. Phys.*, vol. 87, no. 1, pp. 334–344, Jan. 2000, doi: 10.1063/1.371866.

[23] S. Y. Karpov and Y. N. Makarov, "Dislocation effect on light emission efficiency in gallium nitride," *Appl. Phys. Lett.*, vol. 81, no. 25, pp. 4721–4723, Dec. 2002, doi: 10.1063/1.1527225.

[24] E. Kioupakis, P. Rinke, K. T. Delaney, and C. G. Van de Walle, "Indirect auger recombination as a cause of efficiency droop in nitride light-emitting diodes," *Appl. Phys. Lett.*, vol. 98, no. 16, Apr. 2011, Art. no. 161107, doi: 10.1063/1.3570656.

[25] N. Pant, K. Bushick, A. McAllister, W. Lee, C. G. Van de Walle, and E. Kioupakis, "Carrier confinement and alloy disorder exacerbate auger-meitner recombination in AlGaN ultraviolet light-emitting diodes," *Appl. Phys. Lett.*, vol. 125, 2024, Art. no. 021109.

[26] M. Deppner, F. Römer, and B. Witzigmann, "Auger recombination and carrier transport effects in III-nitride quantum well light emitting diodes," *Proc. SPIE*, vol. 8619, pp. 332–341, Mar. 2013.

[27] R. Ishii et al., "Radiative and nonradiative recombination processes in AlGaN quantum wells on epitaxially laterally overgrown ALN/sapphire from 10 to 500k," *Physica Status Solidi (B)*, vol. 20, Mar. 2024, Art. no. 2400018, doi: 10.1002/pssb.202400018.

[28] M. Guttmann et al., "Effect of quantum barrier composition on electro-optical properties of AlGaN-based UVC light emitting diodes," *Semicond. Sci. Technol.*, vol. 34, Jun. 2019, Art. no. 085007.

[29] M. Guttmann et al., "Optical light polarization and light extraction efficiency of AlGaN-based LEDs emitting between 264 and 220 nm," *Japanese J. Appl. Phys.*, vol. 58, no. SC, May 2019, Art. no. SCCB20, doi: 10.7567/1347-4065/ab0d09.

[30] S. Karpov, "ABC-model for interpretation of internal quantum efficiency and its droop in iii-nitride LEDs: A review," *Opt. Quantum Electron.*, vol. 47, no. 6, pp. 1293–1303, Jun. 2015, doi: 10.1007/s11082-014-0042-9.

[31] J. Piprek, "Efficiency droop in nitride-based light-emitting diodes," *Physica Status Solidi (A)*, vol. 207, no. 10, pp. 2217–2225, 2010, doi: 10.1002/pssa.201026149.

[32] A. Kakanakova-Georgieva et al., "MG-doped $AL_{0.85}GA_{0.15}N$ layers grown by *hot-wall* MOCVD with low resistivity at room temperature," *Physica Status Solidi (RRL) – Rapid Res. Lett.*, vol. 4, no. 11, pp. 311–313, 2010, doi: 10.1002/pssr.201004290.

[33] P. Bagheri et al., "Doping and compensation in heavily MG doped Al-rich AlGaN films," *Appl. Phys. Lett.*, vol. 120, no. 8, Feb. 2022, Art. no. 082102, doi: 10.1063/5.0082992.

[34] N. Roccato et al., "Modeling of the electrical characteristics and degradation mechanisms of UV-C LEDs," *IEEE Photon. J.*, vol. 16, no. 1, Feb. 2024, Art. no. 8200206.

[35] J. Hader, J. V. Moloney, and S. W. Koch, "Supression of carrier recombination in semiconductor lasers by phase-space filling," *Appl. Phys. Lett.*, vol. 87, no. 20, 2005, Art. no. 201112, doi: 10.1063/1.2132524.

[36] J. Simon, V. Protasenko, C. Lian, H. Xing, and D. Jena, "Polarization-induced hole doping in wide–band-gap uniaxial semiconductor heterostructures," *Science*, vol. 327, pp. 60–64, 2010.

[37] B. Witzigmann and F. Roemer, "Polarization induced doping for carrier transport in graded III-nitride layers: A simulation study," *Proc. SPIE*, vol. 12415, Mar. 2023, Art. no. 1241502.

[38] T. Kumabe, S. Kawasaki, H. Watanabe, S. Nitta, Y. Honda, and H. Amano, "Space–charge profiles and carrier transport properties in dopant-free GAN-based P-N junction formed by distributed polarization doping," *Phys. Statist. Sol.– Rapid Res. Lett.*, vol. 16, 2022, Art. no. 2200127.